PROCEEDINGS OF SPIE

SPIEDigitalLibrary.org/conference-proceedings-of-spie

Highly sensitive silicon Mach-Zehnder interferometer-based ultrasound sensor

Ouyang, Boling, Li, Yanlu, Kruidhof, Marten, Horsten, Roland, Baets, Roel, et al.

Boling Ouyang, Yanlu Li, Marten Kruidhof, Roland Horsten, Roel Baets, Koen W. A. van Dongen, Jacob Caro, "Highly sensitive silicon Mach-Zehnder interferometer-based ultrasound sensor," Proc. SPIE 11283, Integrated Optics: Devices, Materials, and Technologies XXIV, 112830R (25 February 2020); doi: 10.1117/12.2539573

SPIE.

Event: SPIE OPTO, 2020, San Francisco, California, United States

Highly sensitive silicon Mach-Zehnder interferometer based ultrasound sensor

Boling Ouyang [a,*], Yanlu Li[b,c], Marten Kruidhof[a], Roland Horsten[a], Roel Baets[b,c], Koen W. A. van Dongen[a], and Jacob Caro[a]
[a]Department of Imaging Physics, Delft University of Technology, Lorentzweg 1, 2628 CJ Delft, The Netherlands
[b]Photonics Research Group, Ghent University-imec, Technologiepark-Zwijnaarde 126, 9052 Ghent, Belgium
[c]Center for Nano- and Biophotonics, Ghent University, Technologiepark-Zwijnaarde 126, 9052 Ghent, Belgium

ABSTRACT

We report a highly sensitive ultrasound sensor based on an integrated photonics silicon Mach-Zehnder interferometer (MZI). One arm of the MZI is located on a thin membrane, acting as the sensing part of the device. Ultrasound waves excite the membrane's vibrational mode, thus inducing modulation of the MZI transmission. The measured sensor transfer function is centered at 0.47 MHz and has a −6 dB bandwidth of 21.2%. For 1.0 mW optical input power, we obtain a high sensitivity of 0.62 mV/Pa, a low detection limit of 0.38 mPa/Hz$^{1/2}$ at the resonance frequency and a large dynamic range of 59 dB. In preliminary ultrasound imaging experiments using this sensor, an image of a wire phantom is obtained. The properties of this sensor and the generated image show that this sensor is very promising for ultrasound imaging applications.

Keywords: Integrated photonics sensors, MZI, ultrasound, imaging, MEMS

1. INTRODUCTION

Integrated photonics is an enabling technology for sensing applications in many fields, including environmental, chemical and biomedical sensing[1-4]. Integrated photonics sensors have the advantages of small size, low cost, mass producibility, and electromagnetic immunity. Sensors based on ring resonators (RRs) or Mach-Zehnder interferometers (MZIs) are used in various contexts[1-4] because of their high sensitivity and simple architecture. In response to the agent to be sensed, the well-separated and sharp resonance peaks or dips of a RR or the continuous sinusoidal spectrum of an MZI exhibit a measurable shift, giving the sensor signal. The MZI goes back to the pioneering work of Zehnder and Mach on free space optics interferometers. Integrated photonics MZIs have also been realized in photonic crystals, using self-collimation of light.[5]

Recently, RRs made in polymer and silicon-on-insulator (SOI) platforms have been developed for ultrasound sensing.[6-9] The polymer RRs are located on a rigid substrate. Resonance-wavelength modulation results from the optoelastic effect induced by the ultrasound. The polymer RR sensor is demonstrated for ultrasound in the range of 1-75 MHz, giving a noise equivalent pressure (NEP) of 21.4 Pa.[6] For a small bending radius of the ring, polymers with a higher refractive index than reported are needed. All-optical photoacoustic imaging using a polymer RR sensor has been presented.[7] The RR sensor in SOI[8,9] developed in our department is located on a thin membrane that is sensitive to ultrasound waves. The membrane vibration at the ultrasound frequency leads to the optical sensor signal via transduction by the RR. This sensor shows high sensitivity and a NEP down to 0.4 Pa.[8] However, interrogation of this RR sensor requires special care for two reasons: i) Nonlinear effects occur at moderate optical power, causing bistability of the resonances[10] and ii) The quality factor and the resonance-wavelength positions of the RR are hard to predict because of device-to-device variations inherent to the fabrication process. A membrane-based integrated photonics MZI sensor fabricated in SOI for gas-pressure sensing has been reported.[11] In addition, an optical microphone based on an MZI sensor for acoustic waves in air has been demonstrated, with a working frequency up to 20 kHz.[12]

*B.Ouyang@tudelft.nl

Integrated Optics: Devices, Materials, and Technologies XXIV, edited by Sonia M. García-Blanco, Pavel Cheben, Proc. of SPIE Vol. 11283, 112830R · © 2020 SPIE
CCC code: 0277-786X/20/$21 · doi: 10.1117/12.2539573

Here, we present an on-chip MZI ultrasound sensor fabricated in the SOI platform. The sensing spiral of the MZI is located on a square membrane that was designed to have its vibrational resonance in water at MHz frequencies. With this sensor, we amply extend the operation frequency beyond the ranges in Refs. [11,12] and reach the frequencies of ultrasound imaging. Unlike RRs, MZIs do not exhibit nonlinear effects for relatively high optical input powers, which is advantageous for improving the sensitivity, decreasing the detection limit, and increasing the dynamic range. Benefiting from the gradual transmission characteristic, as opposed to the resonances of a RR, the wavelength-operation range is wider than that of RRs, making the interrogation of the MZI easier and more robust. We report preliminary ultrasound imaging experiments performed with this MZI sensor. These constitute an extension of our previous work on the MZI sensor[13], directed to applications.

2. SENSOR DESIGN AND FABRICATION

A schematic of the MZI sensor is shown in Fig. 1(a). Light of wavelengths around 1550 nm is coupled to the chip via an input grating coupler (GC) and is guided towards two spiral-shaped waveguide arms of different lengths using a 50:50 multi-mode interferometer (MMI). The light leaving the arms is combined in a 2×2 MMI and coupled out by two output GCs. The sensing arm is located on a square membrane, which works as a mechanical resonator with a resonance frequency in the MHz range. The reference arm is on the intact substrate. MZIs of this type were fabricated at IMEC through the Europractice MPW service on a CMOS compatible SOI platform [220 nm Si layer on 2.0 µm buried oxide (BOX)]. The waveguide width is 450 nm. The membrane was obtained using post-processing steps in the Kavli Nanolab Delft. The wafer is first thinned down to 250 µm and then diced. Then, a 0.5 µm thick SiO_2 is deposited per chip as waveguide cladding by plasma-enhanced chemical vapor deposition, followed by low pressure chemical vapor deposition of a 0.15 µm thick Si_3N_4 layer on both chip sides. This Si_3N_4 layer serves as mask in the later etch step of silicon. On the backside of the chip, a square centered at the sensing spiral is opened in the Si_3N_4 layer using optical lithography and reactive ion etching. The membrane is created by locally removing the Si substrate under the spiral using etching in KOH, which stops at the BOX layer. This crystallographic etch yields the typical truncated pyramidal hole shown in Fig. 1(b). The membrane dimension, which is 121 µm × 121 µm for the sensor used in this work, can be accurately controlled by the size of the square window in the Si_3N_4 mask. A microscope image of the membrane region is given in Fig. 1(c), showing accurate alignment of the membrane to the spiral and a precise control of membrane dimension, such that it just matches the spiral size. The length of the spiral is 4.5 mm, ensuring a high sensitivity of the sensor. In the packaging step, the chip is glued on a glass platelet, which seals an air cavity under the membrane. Light is coupled into and out of the chip using two angle polished fibers with a reflective coating on the facet. The fibers are glued on the input and output GCs using UV curable glue.

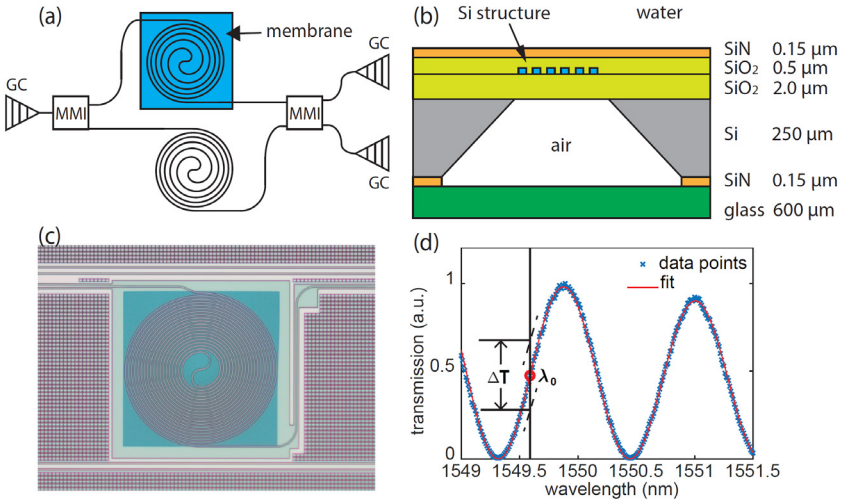

Figure 1. (a) Schematic of the MZI sensor, showing the sensing spiral on the square membrane. (b) Membrane-region cross section of the packaged sensor, with the various layer thicknesses indicated. An air cavity is sealed under the membrane. (c) Microscope image of the membrane region. The side of the square membrane is 121 µm. (d) Normalized transmission spectrum of the MZI sensor. The wavelength-dependent amplitude of the oscillatory transmission is caused by the grating couplers. For operation wavelength λ_0, the transmission modulation ΔT induced by the ultrasound waves is indicated.

The working principle of the MZI ultrasound sensor is of optomechanical nature. Ultrasound waves in the proper frequency bandwidth impinging on the membrane excite its vibrational mode. The membrane vibration induces a modulation of the spiral-waveguide length and of its effective index. These translate to phase modulation of the guided mode arriving at the combiner MMI. For a constant operation wavelength λ_0, this phase modulation results in a modulation of the output power of the MZI. The amplitude of the phase-modulation of the mode arriving at the combiner MMI is

$$\Delta\varphi(\lambda_0, L_s, L_s^*) = \frac{2\pi}{\lambda_0}\left(\int_{L_s^*} n_e^*(\lambda_0, \ell)\,\mathrm{d}\ell - \int_{L_s} n_e(\lambda_0, \ell)\,\mathrm{d}\ell\right), \tag{1}$$

where n_e (n_e^*) and L_s (L_s^*) are the effective index and length of the spiral on the strainless (maximally strained) membrane.

In the experiments, we first measure the regular optical transmission spectrum of the MZI sensor before characterizing its optical response to ultrasound. Near-infrared light of a tunable laser (Santec, TSL-210, step size 10 pm) is coupled to the input GC via a polarization controller (Thorlabs, FPC562) for maximum GC transmission. The wavelength-dependent output power is measured using a photodetector (Newport, 1811-FC-AC). A resulting normalized transmission spectrum is shown in Fig. 1(d). The expected oscillations can be observed in the spectrum, while the smaller amplitude with increasing wavelength results from the wavelength dependence of the GC transmission. The following function is fitted to the normalized spectrum

$$T(\lambda) = (a\lambda + b)\left[\frac{1}{2}\cos\left(2\pi\frac{\lambda}{\mathrm{FSR}} + \Phi(t)\right) + \frac{1}{2}\right]. \tag{2}$$

Here, ($a\lambda$+b) represents the first order approximation of the GC transmission in the used wavelength range. The factor in square brackets is the MZI transmission. λ is the wavelength and FSR is the free spectral range of the MZI. The time-dependent phase $\Phi(t)$ applies when there is ultrasound-induced phase modulation. The resulting fit to the measured spectrum is also shown in Fig. 1(d), giving an FSR of 1.13 nm.

3. CHARACTERIZATION OF THE ACOUSTIC PROPERTIES OF THE SENSOR

The acoustic properties of the MZI sensor are measured using the setup shown in Fig. 2(a). The sensor and a piezo-transducer are coaxially mounted in a U-shaped frame, with 230 mm distance between their faces. The U-shaped frame is submerged in a water tank. An arbitrary waveform generator (Agilent, 33521A) is connected to the transducer, sending a Gaussian modulated sinusoidal voltage pulse towards the sensor. The generated ultrasound pulse in the time domain is given by

$$p(t) = p_0 \exp\left[-\left(\frac{t-\tau_d}{N/(2f_0)}\right)^2\right]\sin(2\pi f_0 t). \tag{3}$$

p_0, τ_d, and f_0 are the pressure amplitude, pulse delay time, and center frequency of the pulse, respectively. The integer N is used to set the pulse length. It also determines the frequency bandwidth of the pulse. Here, we use N = 10 to have a narrow bandwidth of the pulse. The operation wavelength is chosen in the steep part of the MZI transmission [cf. Fig. 1(d)] and the input power of the sensor is set at a constant value. The average optical power transmitted by the MZI is monitored at the DC output of the photodetector for tracking the environmental phase drift of the sensor. During the experiments reported below, this drift is found within ≈ 10 pm. The sensor response to ultrasound pulses is recorded at the AC output of the photodetector, using a 14-bit analog-to-digital converter (ADC, Spectrum, M3i4142-exp). Figure 2(b) shows a typical sensor response to a pulse given by Eq. (3), for p_0 = 32.2 Pa, f_0 = 0.47 MHz (the membrane's resonance frequency; see below) and an input power of 1.0 mW. This response is highly similar to the Gaussian excitation pulse but has an additional tail, which results from the ringing down of the membrane resonance.

The sensor transfer function, i.e., the sensor response as a function of frequency at constant amplitude p_0, is obtained by repeating the measurement of the time response in Fig. 2(b) as a function of frequency, with f_0 increasing from 0.25 to 0.75 MHz, using a 0.01 MHz step size. The actual response at each frequency is calculated as an average of

500 individual responses. The maximum of the signal envelop [see Fig. 2(b)] is taken as the sensor signal at each frequency, calculated using the Hilbert transform of the time response. The frequency characteristic of the transducer is measured using a hydrophone (Precision Acoustics, 1 mm) and is used to remove the frequency dependence of the transducer in the final transfer-function result. We present the resulting normalized transfer function in Fig. 2(c), showing a line shape with two resonances. The dominant resonance has its maximum at 0.47 MHz, which corresponds to the lowest vibrational mode of the membrane. The much weaker sub-resonance at lower frequency may result from a secondary mode related to the dense spiral on the membrane. The −6 dB bandwidth of the dominant resonance is 21.2%.

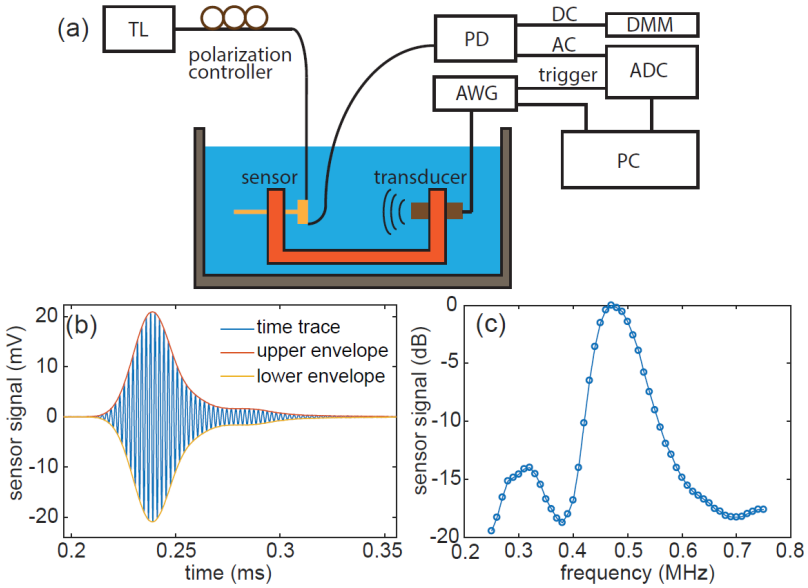

Figure 2. (a) Schematic of the sensor-characterization setup (TL, tunable laser; PD, photodetector; AWG, arbitrary waveform generator; DMM, digital multimeter; ADC, analog-to-digital converter). (b) Measured time response of the sensor to a Gaussian ultrasound pulse with a center frequency of 0.47 MHz. The operation wavelength is chosen to have maximum sensor sensitivity. (c) The measured transfer function of the MZI sensor.

Having obtained the transfer function, we further measure the sensitivity of the sensor at the transfer-function maximum of 0.47 MHz. The wavelength-dependent sensitivity is defined as:

$$S(\lambda) = \alpha I_{\text{in}} \left| \frac{\mathrm{d}T}{\mathrm{d}p} \right| = \alpha I_{\text{in}} \left| \frac{\mathrm{d}T}{\mathrm{d}\lambda} \frac{\mathrm{d}\lambda}{\mathrm{d}p} \right| \approx \alpha I_{\text{in}} \left| \frac{\mathrm{d}T}{\mathrm{d}\varphi} \frac{\Delta\varphi}{\Delta p} \right|. \tag{4}$$

Here, α is the net effect of the loss and gain. I_{in} and p are the input optical power and ultrasound pressure, respectively. Since zero pressure is the reference pressure, Δp equals p. For small values of p, the sensor response is expected to be linear and both $\mathrm{d}\lambda/\mathrm{d}p$ and $\Delta\varphi/\Delta p$ are constant. Therefore, the sensitivity is proportional to I_{in} and $|\mathrm{d}T/\mathrm{d}\lambda|$. The operational wavelength is chosen as 1549.59 nm [indicated in Fig. 1(d)], where $|\mathrm{d}T/\mathrm{d}\lambda|$ and thus the sensitivity are maximum. To obtain the sensitivity, we measure the time response for 33 pressure amplitudes (0.77 – 341 Pa, maximum pressure of 341 Pa is limited by the range of ADC card, not by the sensor itself) of the Gaussian pulse for six optical input powers ranging from 0.5 to 1.0 mW. The averaged time response is bandpass filtered (0.1 – 1.1 MHz, Tukey window) for noise reduction outside the range of interest. The measurement results together with the linear fits presented in Fig. 3(a) clearly show operation of the sensor in the linear response regime for the complete measurement range. The sensitivity for each input power equals to the slope of fitted lines in Fig. 3(a), and ranges from 0.31 to 0.62 mV/Pa. A high degree of linearity of the sensitivity versus optical input power is found in Fig. 3(b), as expected.

The lowest measurable acoustic pressure or NEP is obtained as the root-mean-square (RMS) noise divided by the sensitivity. To measure the RMS noise, we have recorded time traces of the photodetector output during 0.5 ms [i.e., the measuring time also used for the individual time responses contributing to data points in Fig. 3(a)] after each

measurement series of a pressure dependence of the signal amplitude shown in Fig. 3(a), using the same optical power as for these dependencies, but without applying ultrasound and without averaging over multiple results. We use the same bandpass filter. In this way, noise traces are taken under the conditions of the acoustic measurements. From Fig. 3(c), we can see that the RMS noise increases from 0.194 to 0.237 mV in the range of applied powers. This behavior mainly results from an increasing amplification of the intrinsic noise by the increasing optical power. However, the noise-level increase is weaker than the sensitivity increase in Fig. 3(b), causing a notable NEP decrease with increasing power, which is also shown in Fig. 3(c). For 1.0 mW optical input power, the NEP is only 0.38 Pa, corresponding to a detection limit of 0.38 mPa/Hz$^{1/2}$. This NEP and the maximum measured pressure of 341 Pa yields a dynamic range of 59 dB.

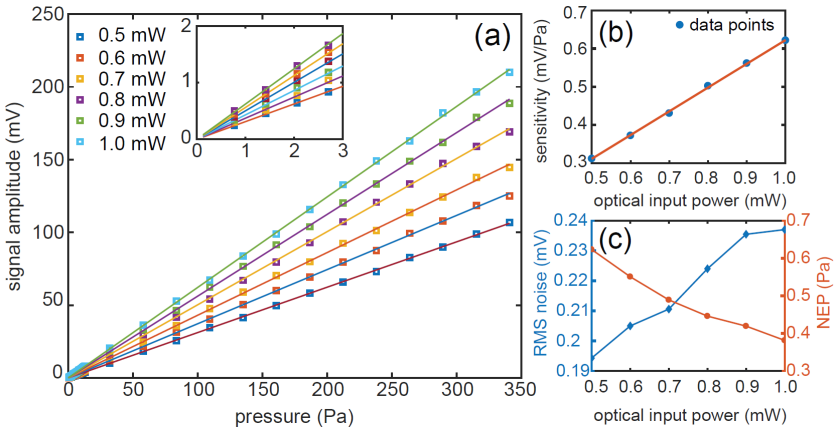

Figure 3. (a) Measured signal amplitude as a function of the amplitude of the acoustic pressure pulse, for different optical input powers. The lines are linear fits to the data points. The inset is a zoom-in of the low pressure range. (b) Sensor sensitivity as a function of the optical input power, together with a linear fit to the data points. (c) Root-mean-square noise (blue) and noise equivalent pressure (red) as a function of the optical input power.

To verify the prediction of the wavelength dependence of the sensitivity in Eq. (4), we follow the same procedure as used for acquiring the sensitivities in Fig. 3(b), using 1.0 mW optical power and operation wavelengths λ_0 in the range 1549.30 – 1550.68 nm, with a 0.06 nm wavelength increment. In this way, we cover one FSR of the MZI transmission. The resulting normalized sensitivity values are plotted in Fig. 4, along with the absolute value of the derivative of the fitted transmission function in Fig. 1(d). Excellent agreement of experiment and theoretical prediction is observed. The curves in Fig. 4 also lead us to the expectation that the sensor is robust to possible misalignment of the wavelength to the operation point of maximum sensitivity, since a misalignment can be easily compensated by increasing the input power without inducing strong nonlinear effects. The rather large FWHM of ≈ 400 pm of the sensitivity branches in Fig. 4, to be compared to FWHM ≈ 100 pm for Si RR sensors[8,9], is of additional help in compensating a misalignment by a power increase.

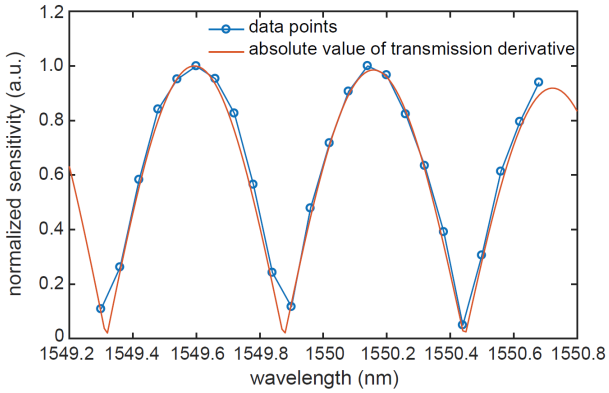

Figure 4. The measured wavelength dependence of the sensor sensitivity. The data points agree excellently with the prediction given by Eq. (4) and the measured transmission in Fig. 1(d).

4. PRELIMINARY ULTRASOUND IMAGING USING THE MZI SENSOR

As a next step, we go beyond characterizing the sensor, by applying it in preliminary pulse-echo ultrasound imaging experiments, to deliver the proof-of-concept of imaging with this type of sensor. We aim to reconstruct an image of a stainless steel wire phantom from pulses sensed by the sensor after backscattered from the wire. The wire diameter is 1.0 mm, smaller than the wavelength of the ultrasound used (≈ 3 mm). Thus, in the imaging plane perpendicular to the wire direction we treat the wire as a point scatterer of ultrasound waves.

We use the synthetic aperture focusing technique[14] (SAFT) for image reconstruction. SAFT is based on delay-and-sum operations. It combines the signals of a series of measurements taken for different pulse-echo geometries of the ultrasound source, phantom and receiver (i.e., sensor). Data summation gives constructive and destructive interference of the measured signals, leading to the reconstructed image. The reconstructed image contrast χ is given by[14]

$$\chi = \sum_{j,t} F_j(t)\, \delta(c_0 t - |\vec{r}^{\,s} - \vec{r}| - |\vec{r}^{\,r} - \vec{r}|). \tag{5}$$

The summation index j numbers the j^{th} measurement. $F_j(t)$ is the scattered pressure field sensed by the sensor for the j^{th} measurement at discrete sampling time t, δ is the Dirac delta function and c_0 is the speed of ultrasound in water, for which we take 1498 m/s. $\vec{r}^{\,s}$, $\vec{r}$ and $\vec{r}^{\,r}$ are the position vectors of the source, wire, and receiver, respectively. In our experiment (see below), we translate the wire, while keeping the source and receiver at constant positions. Thus, $\vec{r}^{\,s}$ and $\vec{r}^{\,r}$ are constant, while $\vec{r}$ varies among the measurement points. This is equivalent to keeping the wire at a constant position and translating the source and receiver simultaneously, while keeping their separation constant.

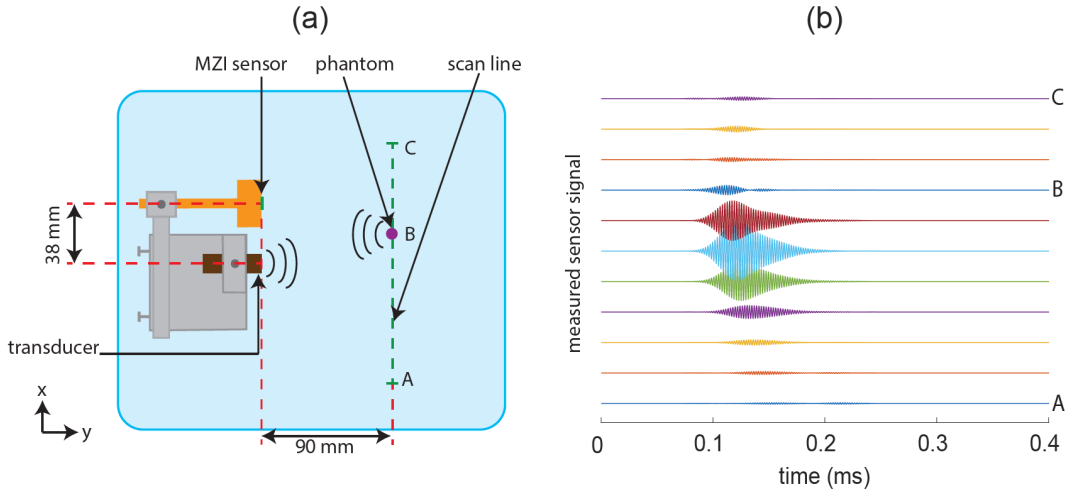

Figure 5. (a) Top view of the ultrasound imaging setup in the water tank. The phantom is a 1.0 mm diameter stainless steel wire that can be scanned in the x-direction along the scan line, from point A to point C. In the figure, the wire is positioned on the scan line at point B, which is on the perpendicular bisector of the line segment connecting the centers of the transducer and the sensor. Positioning the wire at point B gives the shortest time delay between sending and receiving of the pulse. (b) Measured time traces of the sensor signal for different wire position. Between end positions A and C the amplitude of the measured signal first increases and then decreases. For the time delay of the signal this is reversed: it first decreases and then increases.

A top view of the imaging setup, built in a water tank, is given in Fig. 5(a). Using a holder, the sensor and a piezo-transducer acting as source (diameter = 15 mm) are stably mounted in the horizontal imaging plane, with a constant center-to-center distance of 38 mm. The wire is oriented vertically, attached to a scanner. Measurements are taken for multiple wire positions by translating it along the scan line over a distance of 100 mm from point A to point C, with a 1 mm step size. The distance of the scan line to the vertical plane through the faces of the sensor and the transducer is 90 mm, i.e., the wire is always in the transducer's far field. For each wire position, Gaussian ultrasound pulses [see Eq. (3)]

emitted by the transducer arrive at the wire, which backscatters the pulses to the sensor. Using gating, we arrange that pulses arriving at the sensor other than those directly following the path transducer-wire-sensor are excluded from the data processing, i.e., we exclude pulses resulting from direct coupling between transducer and sensor, and from reflections at the walls of the tank, etc.

Examples of measured signals have been plotted in Fig. 5(b). Between the end positions A and C of the scan, the amplitude of the measured signal first increases and then decreases. Since the signal amplitude mainly depends on the magnitude of the scattered field at the sensor, the observed behavior indicates that the arriving scattered field is strongest between positions A and C. Looking in detail, the maximum signal occurs for the wire position on the axis of the transducer. This position corresponds to the maximum pressure received by the wire. Apparently, the total travel distance of the pulse for this wire position being a bit longer than its minimum value and the sensor directivity play a minor role here. The dependence of the signal's time delay on the wire position shows reversed behavior: it first decreases and then increases. This is a geometrical effect. The shortest total travel distance of a pulse and thus the shortest time delay is expected for the wire at point B [see Fig. 5(a)], which is on the perpendicular bisector of the line segment connecting the centers of the transducer and the sensor. Indeed, the time trace in Fig. 5(b) with the shortest time delay was taken for position B.

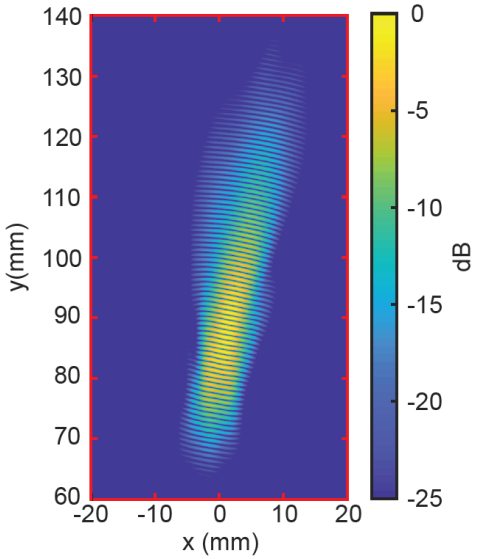

Figure 6. The reconstructed image of the 1.0 mm wire phantom. The lateral and axial resolutions measured at −6 dB are 8 mm and 26 mm, respectively.

In Fig. 6 we present the reconstructed image, which is rather large and elongated, and shows a rotation. The rotation is mainly due to an asymmetry of the sensor-signal strength as a function of wire position. The asymmetry occurs with respect to the reference position defined by the axis of the sensor. Strong signals only occur on one side of the reference, while on the other side rather weak signals occur, an effect seen in the traces of Fig. 5(b). The −6 dB resolution of the image in the x-direction (lateral resolution) and y-direction (axial resolution) are 8 mm and 26 mm, respectively, both much larger than the wire diameter. By analyzing the effect of the various imaging parameters on the resolution in either direction, we have identified ways for improvement. The lateral resolution is mainly limited by the present setup. It can be improved with a modified setup enabling enough measurement points that all yield a proper signal level instead of the present series of wire positions that only partly yield a proper signal level. This can be achieved by using a smaller diameter transducer, which has a wider central lobe of the emitted profile and provides stronger pressure levels further away from the transducer axis. Thus, a much weaker wire-position dependence of the sensor signal is obtained. Another way is keeping the wire position constant on the transducer axis and scanning the sensor. This requires provisions, including polarization maintaining fibers for the packaging of the sensor, to prevent sensor instability due to motion in scanning the sensor as encountered with the present normal fibers. The axial resolution is mainly determined by the

sensor transfer function. The 0.47 MHz resonance frequency and the −6 dB bandwidth of 21.2% of the transfer function lead to a long spatial pulse, limiting the axial resolution. A transfer function with more suitable properties for this wire imaging, in particular a higher resonance frequency and a larger bandwidth, can be obtained as indicated in the next section.

5. DISCUSSION

The sensor properties can be tailored to meet the requirement of certain applications, such as the above imaging experiment or photoacoustic imaging[15], the latter requiring an operation frequency of several MHz and a larger bandwidth. The transfer function of the sensor is determined by the membrane, of which the resonance frequency is proportional to[16] h/d^2, with h and d the thickness and the side of the square membrane, respectively. A ten times increase of the resonance frequency can be easily achieved by changing the membrane dimensions. To obtain a larger bandwidth, the membrane needs to be made lossy, which may be realized by adding a polymer layer on top of the membrane. These adaptations go at the cost of sensitivity. A lower sensitivity can be compensated by using a higher input power, as suggested by Eq. (4). A higher input power also yields a smaller NEP, as shown in Fig. 3(c), giving a larger dynamic range. As the MZI is not a resonator, unlike a RR, there is no field enhancement. Higher optical power may be used without the penalty of strong nonlinear effects. The maximum optical power of 1.0 mW used here for the MZI sensor already induces nonlinear effects in a Si RR sensor.[10] The sensitivity can also be improved by creating a stronger strain response to pressure, for example by increasing the length of the waveguide on the membrane or making the membrane larger and thinner. However, such redesign of the membrane may counteract possible requirements for the transfer function.

6. CONCLUSION

We have demonstrated a highly sensitive silicon MZI ultrasound sensor. The sensing spiral of the MZI is located on a 121 μm × 121 μm membrane that can be brought to resonance in water by applying ultrasound waves. The sensor transfer function, determined by the membrane properties, is centered at 0.47 MHz and has a −6 dB bandwidth of 21.2%. Using 1.0 mW optical input power, we have experimentally obtained a sensitivity of 0.62 mV/Pa, a detection limit of 0.38 mPa/Hz$^{1/2}$, and a dynamic range of 59 dB. As the transmission of the MZI is a relatively weak function of the wavelength, a wide wavelength-operation range is possible. We have applied the sensor in preliminary imaging experiments of a 1.0 mm diameter metallic wire and have delivered the first proof-of-concept of imaging with this type of MZI sensor. The reconstructed image of the wire is rather large in this stage. Proposals for improvement of the resolution of the image in either direction include modification of the imaging setup and sensor characteristics better tailored to the requirements of this imaging task. The merits of the sensor and our first imaging results show that the sensor is promising for imaging applications.

ACKNOWLEDGMENT

The authors gratefully acknowledge the financial support of the Nederlandse Organisatie voor Wetenschappelijk Onderzoek (NWO, project 13534). The authors thank M. Haverdings and P. Kat for valuable discussions, L. Orbe and W. Bogaerts for help in photonics design, B. Mirzaei and J. Gao for use of the scanner, and U. Taskin for use of the ADC system. The Kavli Nanolab Delft is acknowledged for use of fabrication facilities and support.

REFERENCES

[1] Luan, E., Shoman, H., Ratner, D., Cheung, K., and Chrostowski, L., "Silicon photonic biosensors using label-free detection," Sensors 18 (10), 3519 (2018).
[2] Lambeck, P. V., "Integrated optical sensors for the chemical domain," Meas. Sci. Technol. 17 (8), R93 (2006).
[3] Yebo, N. A., Lommens, P., Hens, Z., and Baets, R., "An integrated optic ethanol vapor sensor based on a silicon-on-insulator microring resonator coated with a porous ZnO film," Opt. Express 18(11), 11859-11866 (2010).

[4] De Vos, K., Bartolozzi, I., Schacht, E., Bienstman, P., and Baets, R., "Silicon-on-Insulator microring resonator for sensitive and label-free biosensing," Opt. Express 15(12), 7610-7615 (2007).
[5] Nguyen, H. M., Dundar, M., Van der Heijden, R., Van der Drift, E., Salemink, H., Rogge, S., and Caro, J., "Compact Mach-Zehnder interferometer based on self-collimation of light in a silicon photonic crystal," Opt. Express 18(7), 6437-6446 (2010).
[6] Ling, T., Chen, S.-L., and Guo, L. J., "High-sensitivity and wide-directivity ultrasound detection using high Q polymer microring resonators," Appl. Phys. Lett. 98(20), 204103 (2011).
[7] Hsieh, B.-Y., Chen, S.-L., Ling, T., Guo, L. J., and Li, P.-C., "All-optical scanhead for ultrasound and photoacoustic imaging-Imaging mode switching by dichroic filtering," Photoacoustics 2(1), 39-46 (2014).
[8] Leinders, S., Westerveld, W., Pozo, J., Van Neer, P., Snyder, B., O'Brien, P., Urbach, H., De Jong, N., and Verweij, M., "A sensitive optical micro-machined ultrasound sensor (OMUS) based on a silicon photonic ring resonator on an acoustical membrane," Sci. Rep. 5, 14328 (2015).
[9] Peternella, F. G., Ouyang, B., Horsten, R., Haverdings, M., Kat, P., and Caro, J., "Interrogation of a ring-resonator ultrasound sensor using a fiber Mach-Zehnder interferometer," Opt. Express 25(25), 31622-31639 (2017).
[10] Priem, G., Dumon, P., Bogaerts, W., Van Thourhout, D., Morthier, G., and Baets, R., "Optical bistability and pulsating behaviour in Silicon-On-Insulator ring resonator structures," Opt. Express 13(23), 9623-9628 (2005).
[11] Hallynck, E. and Bienstman, P., "Integrated optical pressure sensors in Silicon-on-Insulator," IEEE Photon. J. 4(2), 443-450 (2012).
[12] Gao, H., Huang, C. H., Westerveld, W., Haouari, R., Troia, B., Verhaegen, F., Jansen, R., Figeys, B., Rottenberg, X., and Rochus, V., "Simulation and characterization of a high-sensitive micro-opto-mechanical microphone," 19th International Conference on Thermal, Mechanical and Multi-Physics Simulation and Experiments in Microelectronics and Microsystems (EuroSimE), Toulouse, (2018).
[13] Ouyang, B., Li, Y., Kruidhof, M., Horsten, R., Van Dongen, K. W. A., and Caro, J., "On-chip silicon Mach-Zehnder interferometer sensor for ultrasound detection," Opt. Lett. 44(8), 1928-1931 (2019).
[14] Ozmen, N., Dapp, R., Zapf, M., Gemmeke, H., Ruiter, N. V., and Van Dongen, K. W. A., "Comparing different ultrasound imaging methods for breast cancer detection," IEEE Trans. Ultrason., Ferroelectr., Freq. Control. 62(4), 637-646 (2015).
[15] Daeichin, V., Wu, M., De Jong, N., Van der Steen, A. F. W., and Van Soest, G., "Frequency analysis of the photoacoustic signal generated by coronary atherosclerotic plaque," Ultrasound in Med. & Biol. 42(8), 2017–2025 (2016).
[16] Leissa, A. W. and Qatu, M. S., [Vibrations of Continuous Systems], McGraw-Hill, 230 (2011).